buildings

MDPI

Article

Behavior of Eccentrically Loaded Concrete-Filled Steel Tube Latticed Columns with Corrugated Steel Plates for Industrial Structures

Xue-Wen Xiao [1], Ning-Ning Zhang [2,*], Xuan Zhao [1,2], Jun Liu [2,3,4], Zhao-Hui Hu [1,2] and Xian Li [2]

[1] CISDI Group Co., Ltd., Chongqing 400013, China; xuewen.xiao@cisdi.com.cn (X.-W.X.); xuan.zhao@cisdi.com.cn (X.Z.); zhaohui.hu@cisdi.com.cn (Z.-H.H.)
[2] School of Mechanics and Civil Engineering, China University of Mining and Technology, Xuzhou 221116, China; liujun@xauat.edu.cn (J.L.); lixian@cumt.edu.cn (X.L.)
[3] School of Civil Engineering, Xi'an University of Architecture and Technology, Xi'an 710055, China
[4] XAUAT Engineering Technology Co., Ltd., Xi'an 710055, China
* Correspondence: tb23030010a41@cumt.edu.cn

Abstract: This paper presents a numerical simulation and theoretical analysis of the eccentric compressive performance of a novel composite concrete-filled steel tube (CFST) latticed column with corrugated steel plates for industrial buildings. The influence of multiple parameters was systematically examined, encompassing the eccentricity ratio, material strengths (steel tube and concrete), corrugated steel plate waveform, and steel lacing tube strength. The results show that eccentric loading causes typical bending failure, with corrugated steel plates providing significant restraining effects, and diagonal lacing tubes optimizing load distribution and bending resistance. Increased eccentricity reduces the load capacity by up to 41.8% but improves the ductility by 50.6%, with benefits ceasing beyond 350 mm of eccentricity. A higher steel strength enhances the load capacity (28.6%) and ductility (14.5%), while a higher concrete strength improves the capacity but reduces the ductility. Longer waveforms in corrugated steel plates improve the stress redistribution, enhancing both capacity (19.1%) and ductility (9.7%). The eccentric compression modification formulas proposed in this study for the latticed column show a reliable calculation accuracy within 11% of simulations.

Keywords: latticed columns; corrugated steel plates; eccentric compression; numerical simulation

check for updates

Academic Editor: Vipul Patel

Received: 10 April 2025
Revised: 13 May 2025
Accepted: 22 May 2025
Published: 23 May 2025

Citation: Xiao, X.-W.; Zhang, N.-N.; Zhao, X.; Liu, J.; Hu, Z.-H.; Li, X. Behavior of Eccentrically Loaded Concrete-Filled Steel Tube Latticed Columns with Corrugated Steel Plates for Industrial Structures. *Buildings* **2025**, *15*, 1788. https://doi.org/10.3390/buildings15111788

Copyright: © 2025 by the authors. Licensee MDPI, Basel, Switzerland. This article is an open access article distributed under the terms and conditions of the Creative Commons Attribution (CC BY) license (https://creativecommons.org/licenses/by/4.0/).

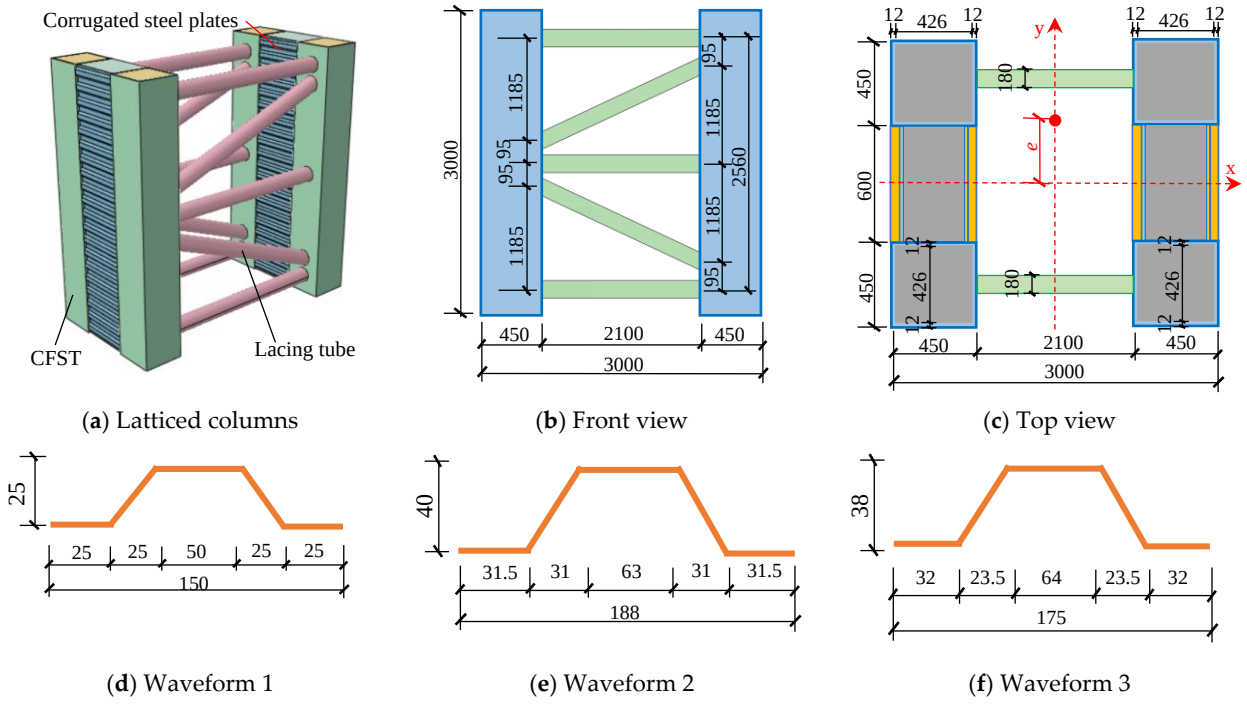
1. Introduction

In industrial settings such as metallurgical facilities, CFST latticed columns are extensively employed due to their suitability for multi-story configurations and extreme loading demands, as shown in Figure 1. Compared with single CFST columns [1], CFST latticed columns, which integrate CFST limb columns by tubular steel braces, exhibit a significantly larger moment of inertia. This enhanced moment of inertia effectively reduces the slenderness ratio of the components, thereby allowing the column limbs to maintain a predominantly axial load-bearing state even under large load eccentricities. Consequently, the full advantages of CFST columns can be fully exploited [2,3]. However, field investigations indicate that latticed columns in many metallurgical industrial buildings exhibit elevated vibration levels under long-term dynamic crane loads, particularly in structures with service periods exceeding 10 years. These vibrations severely impact the normal use and safety of the structures.



Figure 1. Application of CFST latticed column in metallurgical industrial facilities (courtesy of Jun Liu).

A novel composite structural column is proposed to enhance the lateral rigidity and load-bearing performance of latticed CFST columns, capitalizing on the superior shear resistance and out-of-plane stiffness of corrugated steel plates, as illustrated in Figure 2. The composite structural system interlinks neighboring column limbs through dual corrugated steel plates encapsulating concrete cores, while maintaining lacing tube connections for the more widely spaced limbs. This configuration simultaneously addresses spatial constraints of industrial facilities and significantly improves both the structural capacity and lateral rigidity of the composite structural system. The compressive performance of the innovative latticed CFST column has been studied in [4]. To further extend its application, this study examines the structural performance of the proposed CFST latticed system when subjected to eccentric compressive forces.



(**a**) Latticed columns (**b**) Front view (**c**) Top view

(**d**) Waveform 1 (**e**) Waveform 2 (**f**) Waveform 3

Figure 2. Specimen size (unit: mm).

Previous research has demonstrated that the bearing performance of CFST composite latticed columns under eccentric loading is influenced by a variety of factors [5–8]. Wei et al. [9] revealed that the eccentric load-bearing capacity of latticed columns was closely related to the thickness of the steel tube and the strength of the concrete. Jiang et al. [10] and Nie et al. [11] further showed that the slenderness ratio and the eccentricity significantly impacted the eccentric load-bearing capacity of latticed columns, with the column limbs entering the plastic stage upon reaching the ultimate load. Additionally, Ou et al. [12,13] found that under eccentric loading, the contribution of lacing tubes in latticed columns was relatively minor and failed to fully realize their potential. While existing studies indicate that CFST latticed columns exhibit collaborative behavior among column limbs under eccentric loads, there remains room for optimization in terms of load redistribution and overall lateral stiffness improvement in traditional latticed column systems. In recent years, the engineering community has begun to explore the integration of corrugated steel plates as reinforcement components with CFST columns [14], achieving synergistic enhancements in mechanical performance through innovative construction methods. Owing to their unique geometric shape, corrugated steel plates possess high out-of-plane stiffness [15,16], strong bending stiffness [17], excellent synergy with concrete, and good stability [18]. As a result, they have been widely applied in practical engineering projects [19–22].

Despite these advancements, existing studies have predominantly focused on conventional latticed configurations. However, there are still key knowledge gaps in the synergistic interaction mechanisms between CFST latticed columns and corrugated steel plates under eccentric loading conditions. To investigate the synergistic working mechanism between CFST limb columns and corrugated steel plates in the proposed novel composite latticed column, nonlinear finite element modeling (FEM) was implemented in ABAQUS (2020) to simulate the structural response under eccentric compressive forces. Parametric studies evaluated multiple influencing factors: eccentricity ratio, material strengths (steel tubes and concrete), corrugation profiles, and lacing tube strength. Based on these analyses, an eccentric load-bearing capacity estimation model for the column was developed using the results obtained from FEM calculations.

2. FE Model

2.1. Specimen Design

A composite structural specimen was developed for eccentric compression performance investigation, derived from the conventional four-limb laced column configuration prevalent in metallurgical industrial buildings. The specimen featured overall dimensions of 3000 mm (height) × 3000 mm (length) × 1500 mm (width). The structural system was composed of four CFST limb columns. Two corrugated steel plates were incorporated between the two limb columns, with the inter-plate cavities filled with concrete to form composite limbs. The structural integrity was enhanced through strategically positioned steel lacing tubes connecting the main CFST members.

This study evaluated the structural response of CFST composite lattice columns under eccentric loading by developing 14 experimental specimens with variable geometric and material parameters, including load eccentricity ratios, steel tube yield strengths (f_{sy}), concrete strength (f_c), lacing strength (f_L), and the waveform of the corrugated steel plate. Figure 2 illustrates the geometric dimensions of the eccentric compression column specimens. Figure 2c demonstrates the specimen with a loading eccentricity along the positive y-axis, where parameter e denotes the eccentricity distance measured from the centroidal axis to the line of action of the applied load. Tables 1 and 2 summarize the detailed geometric and material parameters. Specimen T1 exhibits the most

representative structural configuration, enabling systematic performance evaluation and comparative analysis.

Table 1. Specimen information.

№	Specimen	Strength of Steel Tube f_{sy} (MPa)	Strength of Concrete f_c (MPa)	Eccentricity e (mm)	Thickness of Lacing Tube t_l (mm)	Strength of Lacing Tube f_L (MPa)	Waveform of Corrugated Plate
1	T1	235	30	350	6	345	Waveform 1
2	E1	235	30	150	6	345	waveform 1
3	E2	235	30	250	6	345	waveform 1
4	E3	235	30	450	6	345	waveform 1
5	C1	400	40	350	6	345	waveform 1
6	C2	400	50	350	6	345	waveform 1
7	H1	300	30	350	6	345	waveform 1
8	H2	355	30	350	6	345	waveform 1
9	H3	400	30	350	6	345	waveform 1
10	B1	355	30	350	6	345	waveform 2
11	B2	355	30	350	6	345	waveform 3
12	LQ1	235	30	350	6	235	waveform 1
13	LQ2	235	30	350	6	345	waveform 1
14	LQ3	235	30	350	6	400	waveform 1

Note: The waveform of the corrugated plate is shown in Figure 2.

Table 2. Geometric parameters of specimens.

	Steel Tube $B_s \times t_s$ (mm)	Corrugated Plate Width B_c (mm)	Corrugated Plate Thickness t_c (mm)	Lacing Tube Diameter D (mm)	Lacing Tube Thickness t_L (mm)
T1	□450 × 12	600	1.2	180	6

Note: The dimensional parameters are defined as follows: B_s: the width of the steel tube; t_s: the thickness of the steel tube; t_c: the thickness of the corrugated plate; D: the diameter of the lacing tube; t_L: the thickness of the lacing tube.

2.2. FEM Approach and Boundary Constraints

This study developed FE models for the latticed column using ABAQUS FEA software, illustrated in Figure 3. Steel tubes, lacing tubes, concrete, and corrugated steel plates were discretized with C3D8R solid elements. Following mesh sensitivity studies, a 40 mm global element size was selected, with critical regions refined to 20 mm. The concrete–steel interface interaction was modeled using a surface-to-surface contact formulation, assigning a 0.2 friction coefficient to tangential interactions. Tie constraints governed connections between steel tubes, lacing members, and corrugated plates. Coupling points were established at column extremities to apply boundary constraints and displacement loads. The base support was modeled as a fixed hinge connection, restraining all translational degrees of freedom (U1 = U2 = U3 = 0) while permitting free rotation about the vertical axis (UR3 $\neq$ 0). At the column top, a vertical displacement load (U2 = -30 mm) was applied, with lateral translations (U1 = U3 = 0) and horizontal rotations (UR1 = UR2 = 0) constrained. Crucially, rotation about the longitudinal axis (UR3) remained unrestrained at both ends to replicate realistic semi-rigid connections in latticed column systems.

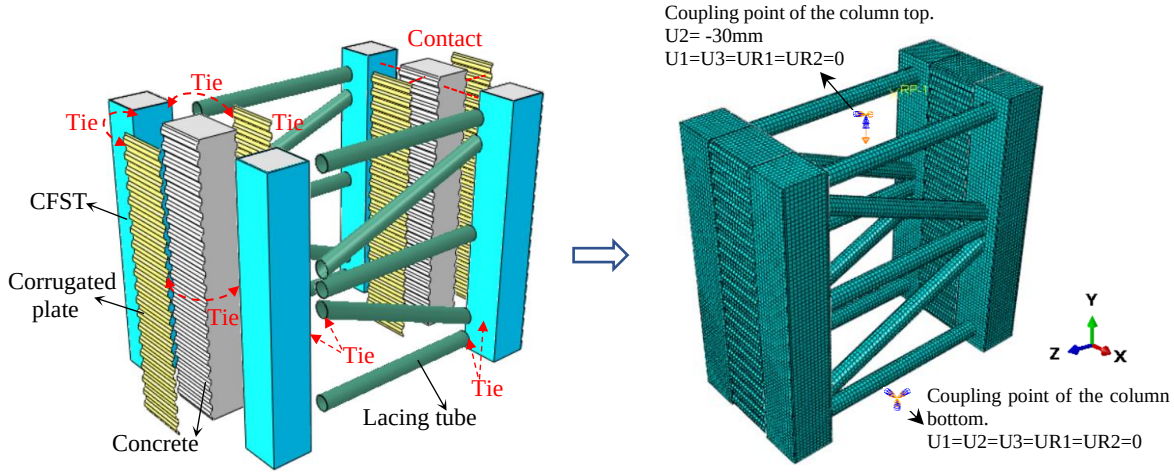


Figure 3. FE models of the latticed column.

2.3. Material Constitutive Model

2.3.1. Concrete

Concrete material behavior was simulated using Liu's confinement-modified stress–strain law [23], capturing the enhanced compressive behavior from steel–concrete interaction.

$$y = \begin{cases} 2x - x^2 & (x \le 1) \\ \frac{x}{\beta_0 (x-1)^{\eta} + x} & (x > 1) \end{cases} \tag{1}$$

where $x = \frac{\varepsilon}{\varepsilon_0}$; $y = \frac{\sigma}{\sigma_0}$; $\sigma_0 = f_c$; and σ_0, ε_0, σ, and ε are the peak stress, peak strain, stress, and strain of concrete, respectively.

2.3.2. Steel

Steel material nonlinearity was modeled using Esmaeily et al.'s constitutive model [24]. The fracture behavior of steel was considered by incorporating damage evolution into the steel constitutive model. As suggested by Yu et al. [25], the correlation between equivalent plastic damage strain and stress triaxiality (η) adopts the simplified piecewise formulation, as expressed in Equations (2) and (3).

$$\bar{\varepsilon}_0^{pl} = \begin{cases} \infty & (\eta \le -1/3) \\ C_1/(1+3\eta) & (-1/3 \le \eta \le 0) \\ C_1 + (C_2 - C_1)(\eta/\eta_0)^2 & (0 \le \eta \le \eta_0) \\ C_2\eta_0/\eta & (\eta_0 \le \eta) \end{cases} \tag{2}$$

$$C_1 = C_2\left(3^{1/2}/2\right)^{1/n} \tag{3}$$

where C_1 represents the equivalent plastic damage strain of steel plates under shear-dominated loading (η = 0), while C_2 denotes the equivalent plastic damage strain in a gape round steel tubes subjected to uniaxial tension ($\eta = \eta_0$). Bao et al. [26] established that η_0 approximates 1/3. The parameter C_2 is calculated as $-\ln(1 - AR)$, where AR corresponds to the diminished cross-sectional area within the necking region of axisymmetric tensile specimens.

The constitutive relationship for steel incorporating plastic damage effects becomes active once the equivalent plastic strain limit is attained. Steel damage progression is

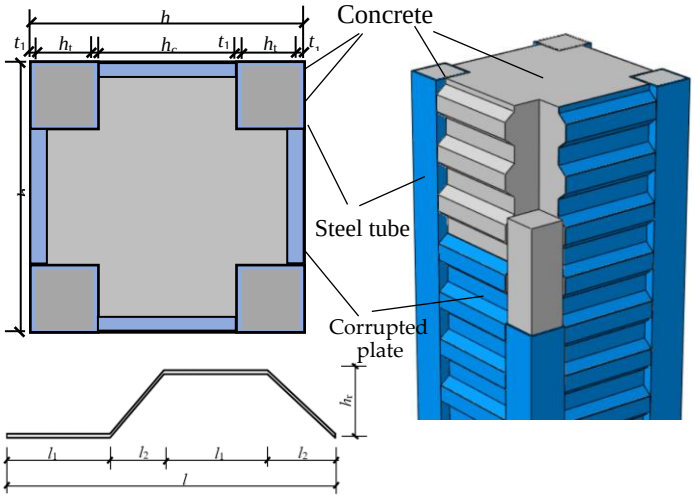
governed by damage factor D (Equation (4)), where D = 0 indicates the undamaged material state and D = 1 corresponds to complete material failure.

$$D = 1.3\left(\frac{\overline{\mu}^{pl}}{\overline{\mu}_f}\right)^{7.6} \tag{4}$$

where $\overline{\mu}_f$ is the ultimate strain of steel after tensile fracture and $\overline{\mu}^{pl}$ is the plastic strain.

3. Validation of the FE Model

To verify the proposed constitutive material model and simulation methodology, this study analyzes the eccentric compressive performance of concrete-filled horizontal corrugated steel plate tubular composite columns (CFHCSPTCs) referenced in Ref. [27]. Figure 4 displays the test specimen's geometric parameters and structural layout.

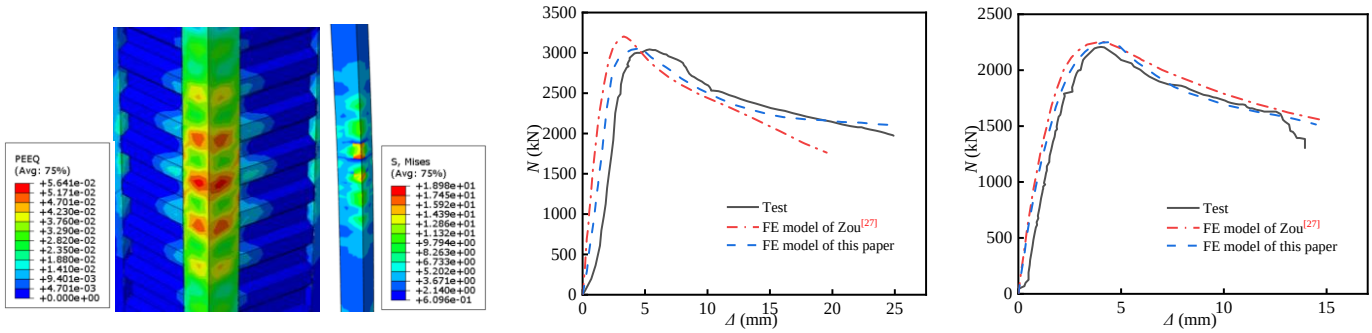


Height of column	1400
Eccentricity of specimen C1	49.5
Eccentricity of specimen C2	99
h	350
h_t	69
h_c	200
t_1	3
t_2	1
l_1	31.5
l_2	1

(Unit: mm)

Figure 4. The size of the column CFHCSPTCs.

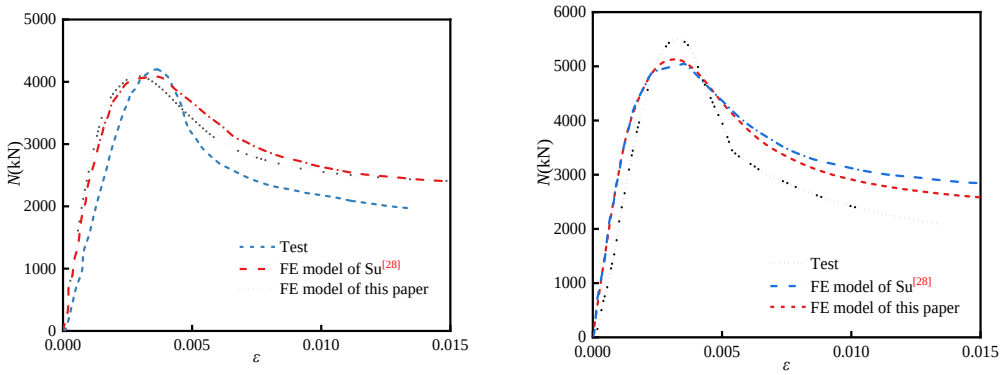
Figure 5 compares the deformation results obtained from numerical simulations and tests of columns under eccentric compression and presents the load–displacement curves from both tests and numerical simulations under eccentric loading. The simulated and test curves demonstrate similar trends, with peak load discrepancies of only 0.6% for specimen C1 and 1.6% for specimen C2, indicating close consistency between the numerical and test results.



(**a**) Failure phenomenon (**b**) C1 (**c**) C2

Figure 5. Simulation verification of Zou (2021) [27].

This study also analyzes the compressive performance of angle steel-corrugated steel plate confined concrete columns referenced in Ref. [28]. Comparative analysis of the load–strain curve of tests and numerical simulations, illustrated in Figure 6, reveals remarkable agreement in their mechanical responses. The peak load differences between simulation and test measurements are merely 2.3% and 7.4% for specimens A1.5-45-5-350 and A1.5-45-5-400, respectively, demonstrating close consistency between numerical predictions and actual test data.



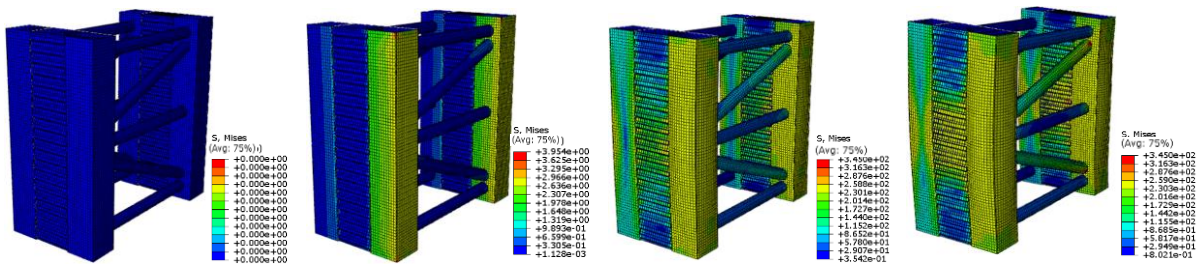
(**a**) A1.5-45-5-350 (**b**) A1.5-45-5-400

Figure 6. Simulation verification of Su (2025) [28].

4. Simulation Results and Analytical Assessment

4.1. Failure Modes

Figure 7 illustrates the strain–deformation evolution process of the typical specimen T1 under eccentric compressive loading. In the early phase of load application, the structural member maintains linear elastic behavior in the elastic working phase, demonstrating negligible global distortion with optimal component interaction (Figure 7a). With progressive load escalation, the specimen enters an elastoplastic stage (Figure 7b), characterized by pronounced stress redistribution phenomena. The compressive area at the column top reaches the yield strength first, and the stress propagates from the top to all of the column. Simultaneously, the tensile area of the column commences resisting tensile stresses through the composite action due to the synergistic restraint effect of the corrugated plate and concrete. A distinct stress concentration area emerges near the interfacial transition region of corrugated steel to steel tubular components, mainly resulting from altered stress transmission mechanisms.



(**a**) Initial loading stage (**b**) Elastoplastic stage (**c**) Plastic stage (**d**) Final loading stage

Figure 7. Deformation of specimen during loading process.

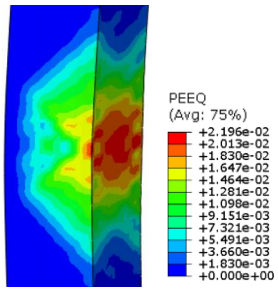
With further loading, the specimen progresses into the plastic deformation phase (Figure 7c). In this stage, the mechanical behavior of the specimen exhibits pronounced nonlinear characteristics, the core concrete in the compressive area undergoes expansion

failure under complex stress states, and the outer steel tube experiences buckling deformation due to weakened confinement. In the tension area, the strain in the steel tube concrete continues to increase, and the restraining effect of the corrugated steel plate is fully utilized, inducing significant stress escalation coupled with extensive deformations. As illustrated in Figure 7d, the final failure mode reveals a distinct bending deformation pattern under eccentric compressive loading. The CFST column in the compressive area undergoes significant compressive deformation and local buckling, while the tensile strain concentrates in the middle region. The interfacial area connecting the corrugated steel plate and the steel tube maintains a high strain level, with the strain showing a tendency to concentrate toward the middle region. Notably, compared to the horizontal lacing tubes, the diagonal lacing tubes exhibit a more pronounced stress concentration effect. This phenomenon indicates that under eccentric compressive loading, the diagonal lacing tubes, through their unique spatial arrangement, provide more effective restraint to the column limbs, thereby significantly enhancing the overall bending resistance and deformation capacity of the latticed column. This mechanical behavior fully reflects the collaborative working mechanism and stress transfer path of the proposed latticed columns under eccentric compressive loading.

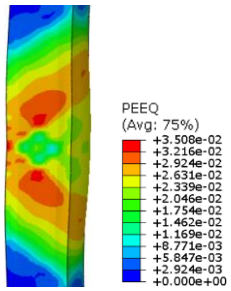
4.2. Parameter Analysis

4.2.1. Eccentricity

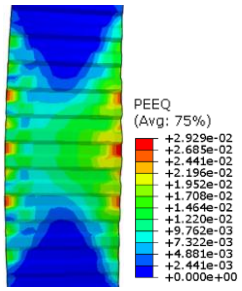
Figure 8 illustrates the damage modes of various elements of the specimen under eccentric loading with different eccentricity ratios. With the progressive increase in load eccentricity, the overall flexural deformation of the specimen becomes significantly more pronounced, and the stress and strain distribution of each component exhibits distinct asymmetric characteristics.



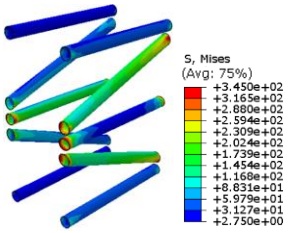
(**a1**) Steel tube on the tension area



(**a2**) Steel tube in the compression area

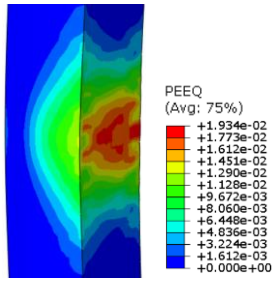


(**a3**) Corrugated plate

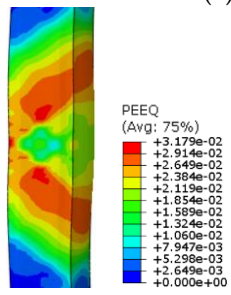


(**a4**) Lacing tube

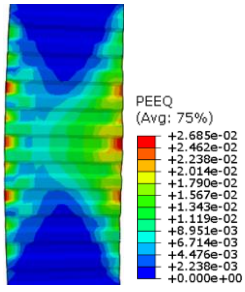
(**a**) e = 50 mm



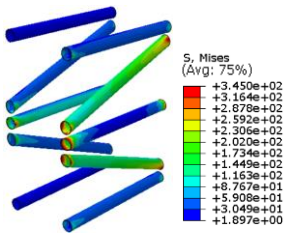
(**b1**) Steel tube on the tension area



(**b2**) Steel tube in the compression area



(**b3**) Corrugated plate



(**b4**) Lacing tube

(**b**) e = 150 mm

Figure 8. *Cont.*

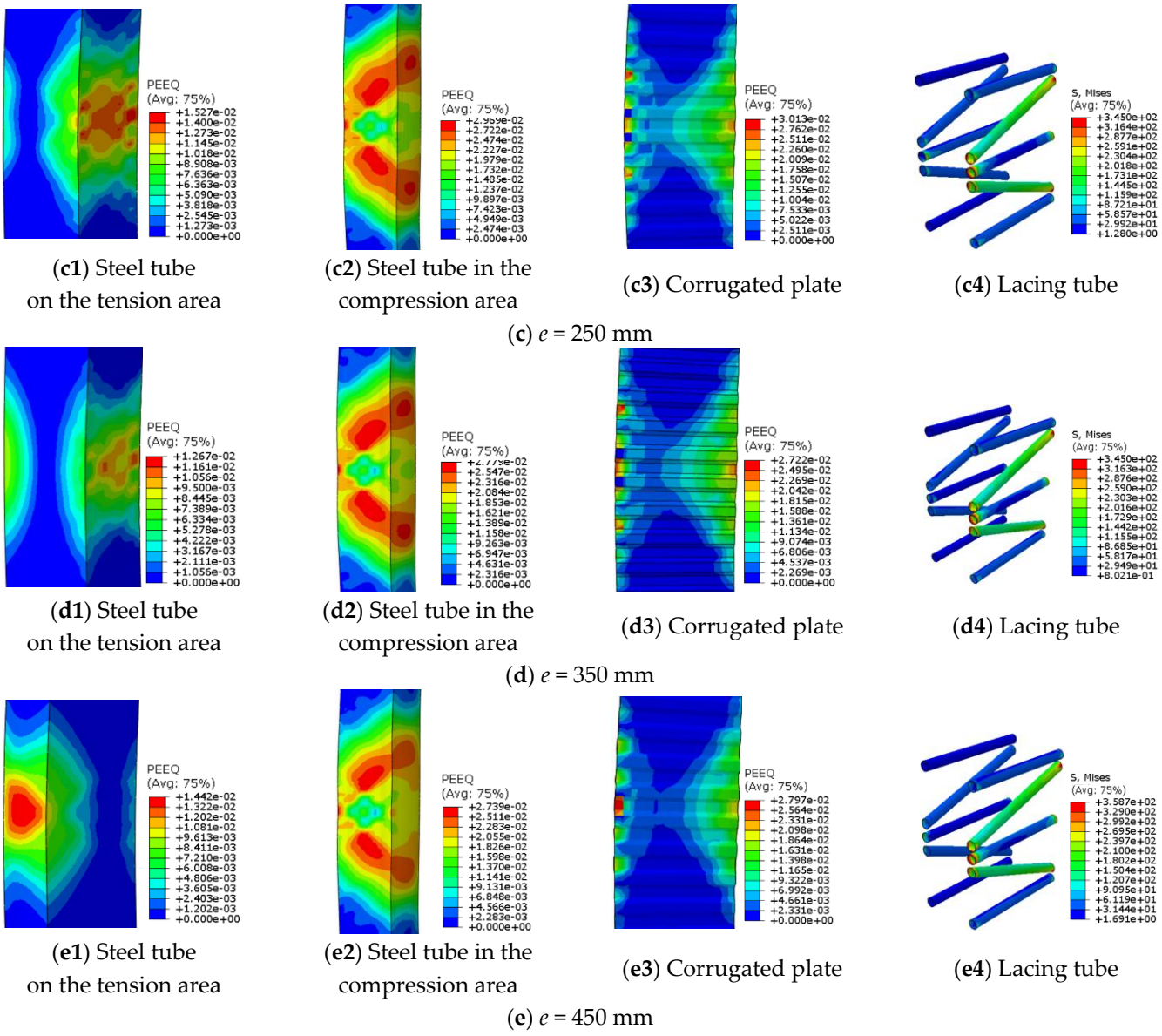


Figure 8. Failure modes of specimens with different eccentricity ratios.

Under eccentric loading, the steel tube in the tension area exhibits significant bending deformation, with the strain predominantly localized in the mid-region. With increasing load eccentricity, the overall flexural moment of the specimen increases, leading to intensified tensile strain in the outer area of the steel tube in the tension area. Meanwhile, the inner area of the steel tube gradually unloads due to changes in bending curvature. The development of plasticity in the steel tube further concentrates the strain distribution toward the outer area. Therefore, the strain in the inner area of the steel tube in the tension area gradually decreases, while the strain in the outer area increases.

Under increasing load, the steel tube and concrete in the compression area are subjected to heightened compressive stress. The concrete gradually reaches its compressive strength and undergoes crushing failure, which weakens the restraining effect of the outer steel tube and subsequently triggers local buckling deformation.

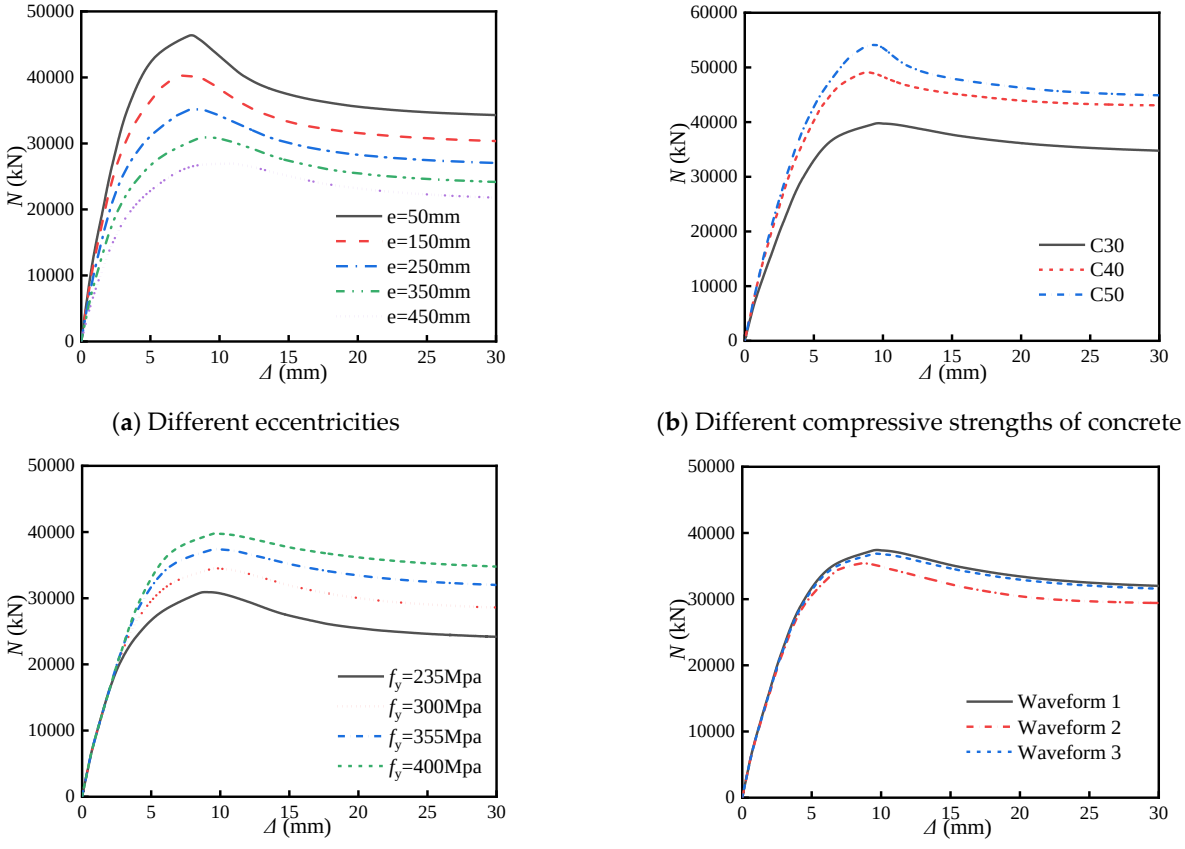
As shown in Figure 8, a pronounced diagonal strain band forms in the mid-region of the compression-area steel tube, and this band expands further with increasing eccentricity. This phenomenon occurs because, under eccentric loading, the steel tube in the compression area is not only subjected to axial compression but also experiences significant shear

stress. This is due to the fact that the compression-area steel tube is not only under axial compression but also experiences substantial shear stress under eccentric loading.

The corrugated steel plate demonstrates a notable restraining effect under eccentric loading. As depicted in Figure 8, substantial strain develops along the contact surface of the profiled corrugated steel plate and the steel tube, gradually spreading toward the mid-region and ultimately forming a distinct X-shaped strain band. With increasing eccentricity, the compressive strains in the corrugated steel plate rise significantly, while the strain in the tension area decreases relatively. This behavior is attributed to the unique corrugated structure of the steel plate, which transfers load from the compression area to the tension area, thereby coordinating the deformation between the steel tube and encased concrete.

The stress distribution in the lacing tubes highlights the critical role of the diagonal lacing tubes under eccentric loading. Stress is predominantly concentrated in the diagonal lacing tubes in the compression area, demonstrating their effectiveness in transferring loads through their spatial configuration and providing additional lateral support to the column limbs. This stress distribution further underscores the critical contribution made by diagonal lacing tubes toward enhancing system-level mechanical behavior in the latticed column.

Figures 9a and 10a demonstrate that the load eccentricity exerts substantial influence on mechanical behavior. With the progressive elevation in eccentricity, both ultimate strength and initial stiffness exhibit consistent reduction, while the ductility coefficient increases. This indicates that larger eccentricities lead to a more pronounced bending deformation in the specimens, accompanied by an enhanced non-uniformity in cross-sectional stress distribution and increased bending effects.



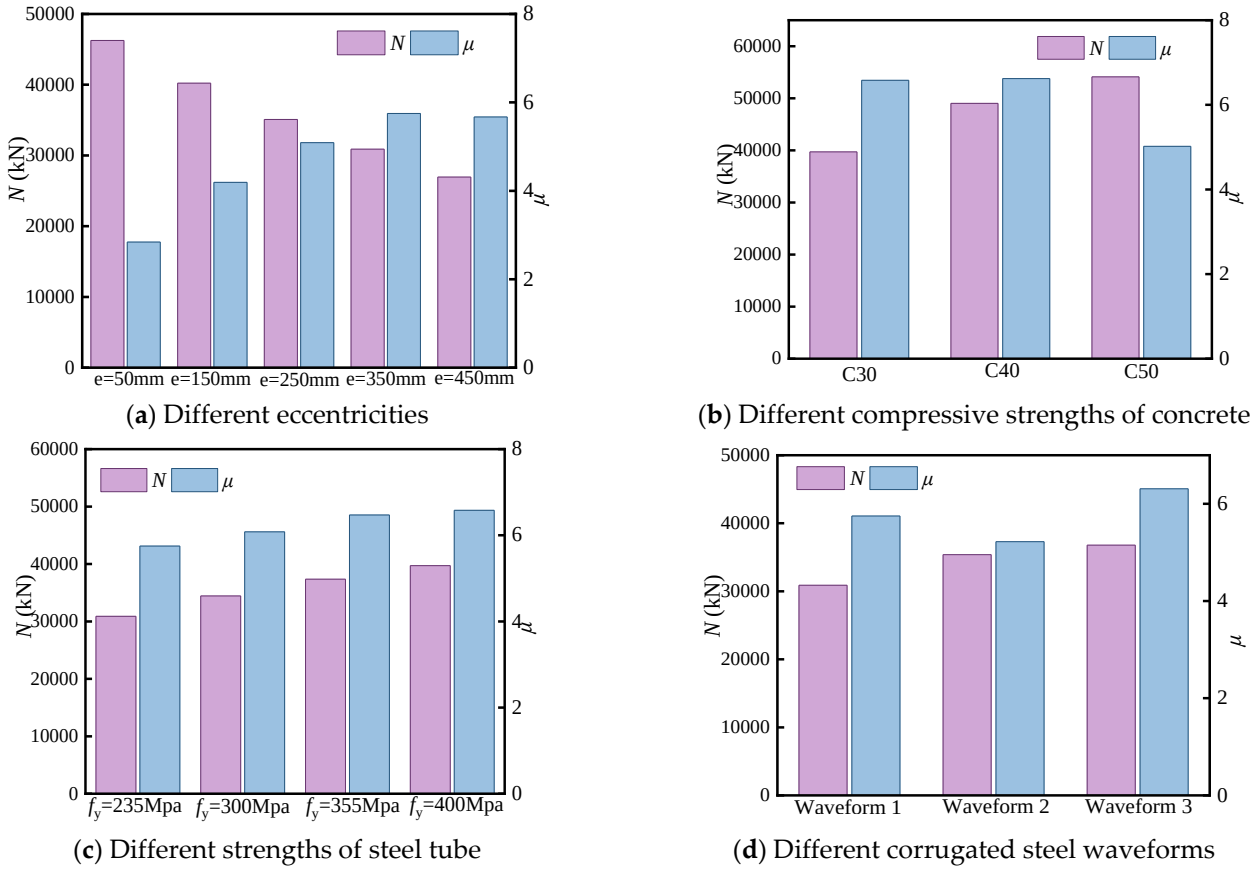
(**a**) Different eccentricities

(**b**) Different compressive strengths of concrete

(**c**) Different strengths of steel tube

(**d**) Different corrugated steel waveforms

Figure 9. Load–displacement curves of specimens.



(**a**) Different eccentricities

(**b**) Different compressive strengths of concrete

(**c**) Different strengths of steel tube

(**d**) Different corrugated steel waveforms

Figure 10. N_y and μ comparison.

The data presented in Table 3 reveal that the eccentricity of specimen E4 is 9 times that of specimen E1, while its load-bearing capacity decreases by 41.76%. This suggests that eccentric loading limits the contribution of the tensile area to the overall load-bearing capacity. Meanwhile, the eccentricity of specimen T1 is 7 times that of specimen E1, and its ductility coefficient increases by 50.61%. This is primarily attributed to the enhanced bending effect caused by the increased eccentricity, which shifts the stress distribution toward the compression area, thereby providing greater strain development space for the steel in the tensile area and improving the deformation capacity of the member. Notably, when the eccentricity exceeds 350 mm, the ductility coefficient of the specimens no longer continues to increase. This is because, with further increases in eccentricity, failure mechanisms transition from strength-governed to stability-dominated, limiting the development of cross-sectional plasticity. Additionally, the concrete within compressive areas attains peak strain prior to steel yielding, restricting the full yielding of the steel. Therefore, it is essential to appropriately control the magnitude of eccentricity in practical engineering applications to ensure that the structure maintains both adequate load-bearing capacity and sufficient ductility.

Table 3. Numerical simulation results of eccentric compression for each specimen.

Specimen	Eccentricity e (mm)	Strength of Steel Tube f_{sy} (MPa)	Strength of Concrete f_c (MPa)	Thickness of Lacing Tubes t_1 (mm)	Strength of Steel Tube f_L (MPa)	N_P (kN)	μ
T1	350	235	30	6	345	30,892.8	5.75
E1	50	235	30	6	345	46,259.9	2.84
E2	150	235	30	6	345	40,224.3	4.19

Table 3. *Cont.*

Specimen	Eccentricity e (mm)	Strength of Steel Tube f_{sy} (MPa)	Strength of Concrete f_c (MPa)	Thickness of Lacing Tubes t_l (mm)	Strength of Steel Tube f_L (MPa)	N_P (kN)	μ
E3	250	235	30	6	345	35,089.1	5.09
E4	450	235	30	6	345	26,942.5	5.67
C1	350	400	40	6	345	49,030.7	6.62
C2	350	400	50	6	345	54,117.7	5.02
H1	350	300	30	6	345	34,442.3	6.08
H2	350	355	30	6	345	37,349.8	6.47
H3	350	400	30	6	345	39,718.9	6.58
B1	350	235	30	6	345	35,379.9	5.22
B2	350	235	30	6	345	36,788.9	6.31
LQ1	350	235	30	6	235	30,771.4	5.73
LQ2	350	235	30	6	300	30,771.5	5.75
LQ3	350	235	30	6	400	30,771.5	5.76

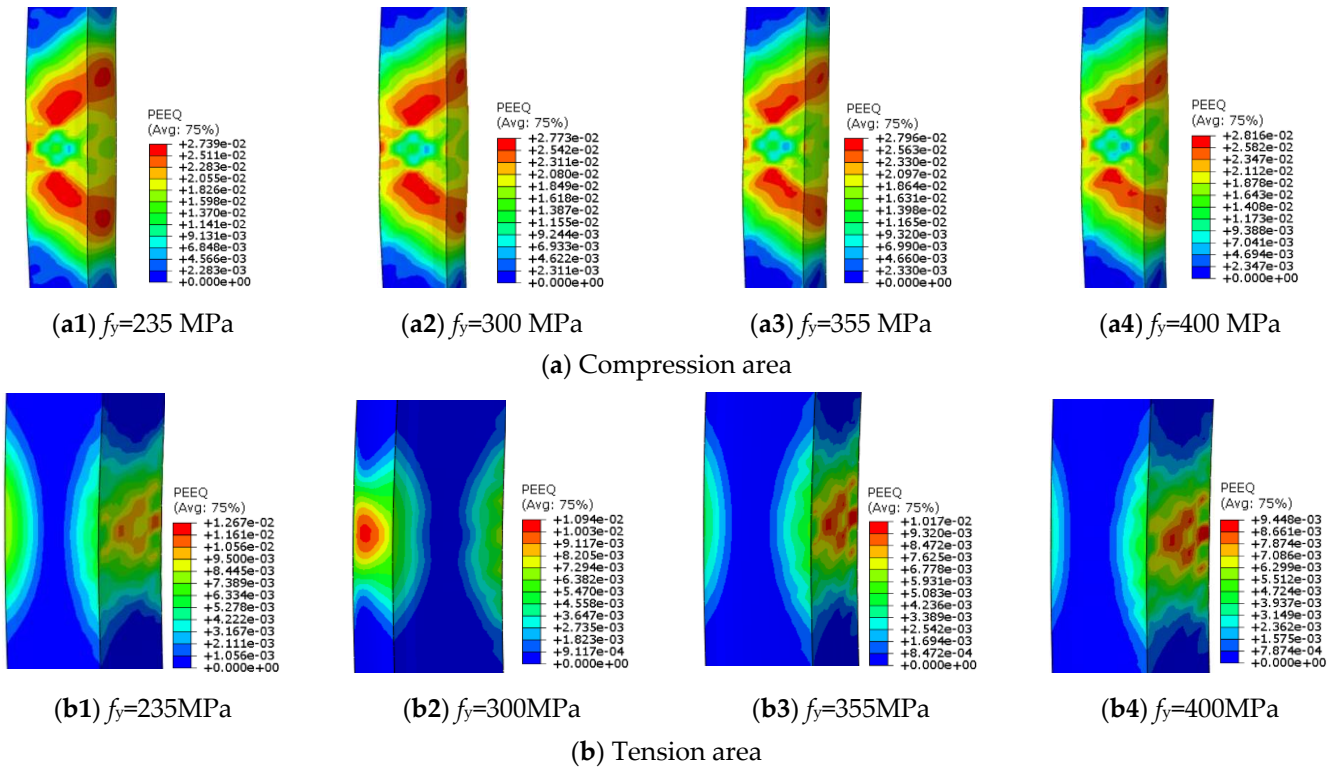
Note: N_P and μ are the peak load and ductility coefficient of the specimens, respectively.

4.2.2. Strength of Concrete

Figure 8b illustrates the load–displacement curves of specimens with different concrete strengths under eccentric loading. The load-bearing capacity of the specimens gradually increases with the improvement in concrete strength. Figure 9b further demonstrates that while the load-bearing capacity of the specimens significantly improves with higher concrete strength, the ductility coefficient exhibits a declining trend. According to the data in Table 3, compared to the specimen with C30 concrete, the load-bearing capacities of the specimens with C40 and C50 concrete increase by 23.44% and 36.25%, respectively. This demonstrates that increased concrete strength directly enhances load capacity. Notably, compared to the C30 concrete specimen, the ductility of the C40 concrete specimen remains almost unchanged, while that of the C50 concrete specimen decreases by 23.71%. This suggests that although C50 concrete significantly enhances the load-bearing capacity, it exhibits pronounced brittle failure characteristics. Comparative analysis reveals that the composite action of C40 concrete–steel systems simultaneously enhances resistance while preserving adequate deformation capacity. Therefore, the design of eccentrically compressed lattice columns must fully complete the synergistic deformation between concrete and steel in practical engineering to achieve a balance between load-bearing capacity and ductility.

4.2.3. Strength of Steel Tube

As shown in Figure 11, the stress distribution across the specimen cross-section exhibits significant non-uniformity under eccentric loading, leading to distinct failure modes in the steel tubes located in the compression area and tension area. For the steel tube in the compression area, the failure process is characterized by the progressive development of local buckling. Local buckling of the steel tube reduces the confinement effect on the core concrete in the initial stage, leading to a decrease in the supporting capacity of the concrete. This, in turn, exacerbates the plastic deformation and local buckling of the steel tube. When the steel tube has higher strength, the onset of local buckling in the compression area is delayed, but the ultimate failure still manifests as a coupling effect of local buckling and global instability. In contrast, the steel tube in the tension area primarily experiences bending deformation and local buckling under eccentric loading. As the stiffness of the steel tube increases, its deformation capacity is significantly enhanced.



(**a1**) f_y=235 MPa (**a2**) f_y=300 MPa (**a3**) f_y=355 MPa (**a4**) f_y=400 MPa

(**a**) Compression area

(**b1**) f_y=235MPa (**b2**) f_y=300MPa (**b3**) f_y=355MPa (**b4**) f_y=400MPa

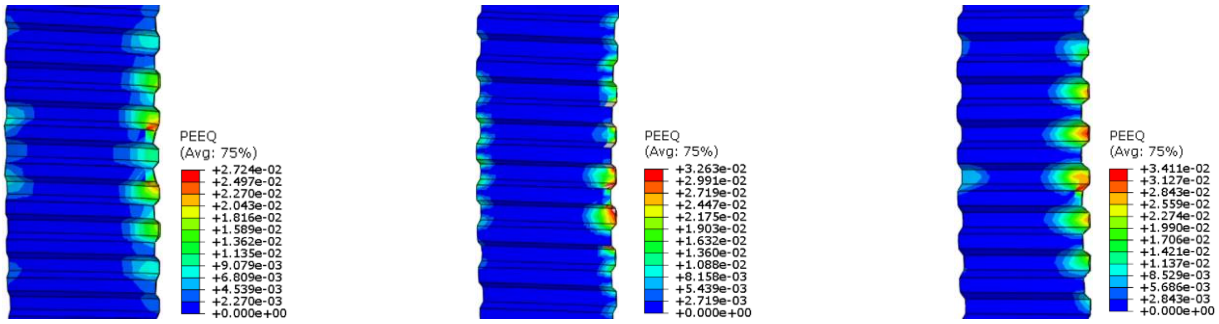
(**b**) Tension area

Figure 11. Equivalent plastic strain of steel tubes.

As shown in Figures 9c and 10c, the load-bearing capacity and ductility of the specimens exhibit an increasing trend with the enhancement in steel strength. According to the data in Table 3, increasing the steel strength from 235 MPa to 400 MPa results in a 28.57% improvement in load-bearing capacity and a 14.45% increase in ductility of specimen. This improvement is primarily attributed to the enhanced stress redistribution capacity of high-strength steel tubes in both the compression area and tension area, as well as their effective suppression of local buckling deformation. However, excessively high steel strength may cause the concrete in the compression area to reach its ultimate compressive strain before the steel tube in practical engineering applications, leading to concrete crushing and sudden failure of the component. Therefore, it is essential to appropriately match the strength of steel tubes in the compression area and tension area to ensure that the component exhibits both excellent load-bearing performance and ductility under eccentric loading in practical design.

4.2.4. Waveform of Corrugated Plate

Figure 12 illustrates the distribution of equivalent plastic strain for corrugated steel plates under eccentric loading with different waveforms. The plastic strain is primarily concentrated at the connection between the corrugated plate and the steel tube. This indicates that the plastic deformation of the corrugated steel plate under eccentric loading predominantly occurs in regions of highest stress concentration. Specifically, the specimen with waveform 2 exhibits the least deformation, with the plastic strain most concentrated at the connection between the compressed region and the steel tube. This reflects the higher rigidity of this waveform, suggesting that it has better resistance to deformation and can effectively withstand localized plastic deformation. In contrast, the specimen with waveform 1, having the largest plastic deformation area, shows that this waveform is more prone to localized yielding under loading, resulting in more noticeable deformation.



(**a**) Waveform 1 (**b**) Waveform 2 (**c**) Waveform 3

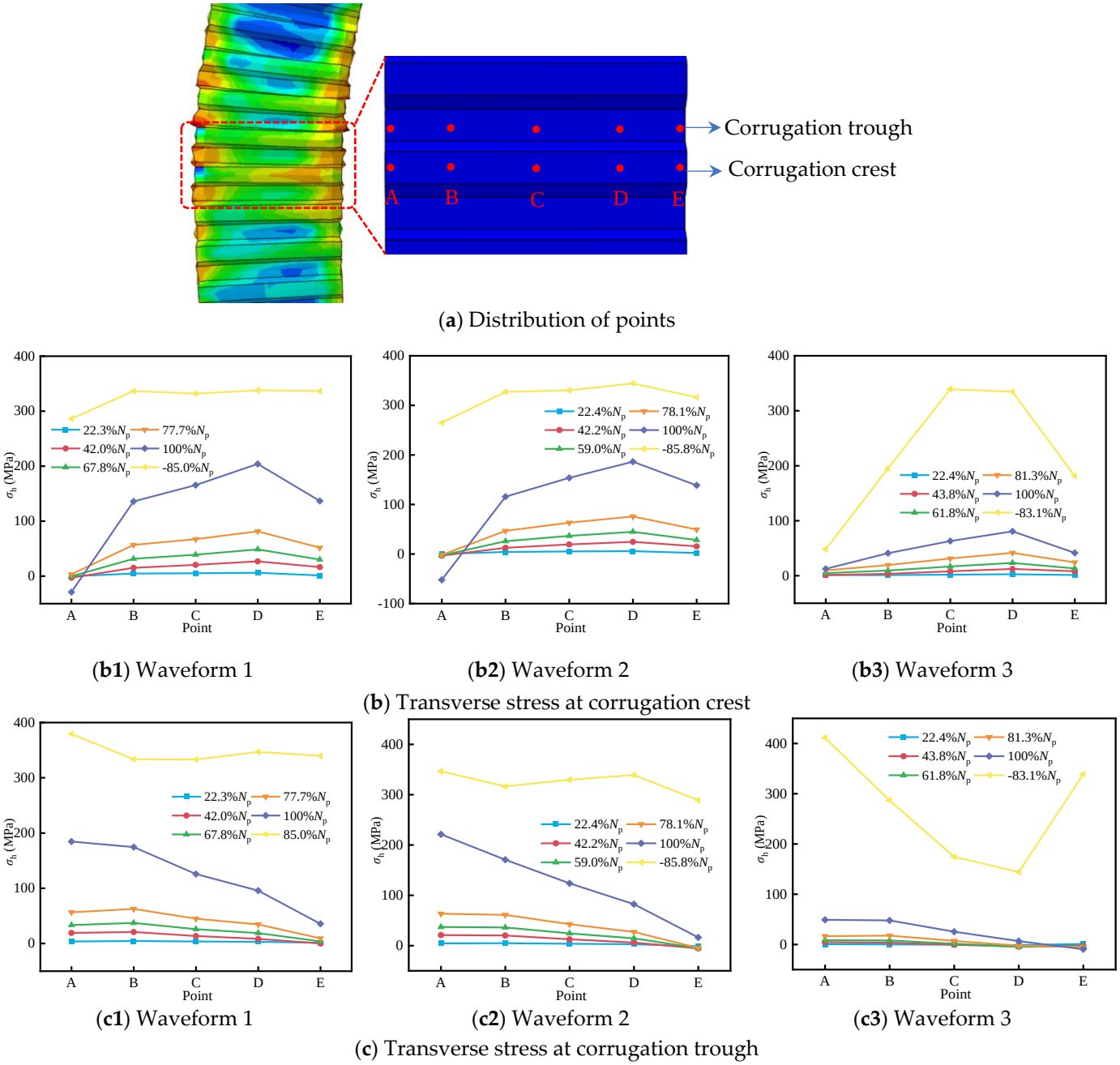
Figure 12. Equivalent plastic strain of corrugated steel plate.

As shown in Figures 9d and 10d, the bearing capacity of the specimens increases with the wavelength. According to the data in Table 3, the specimen with waveform 3 exhibits a 9.7% improvement in ductility and a 19.1% increase in bearing capacity compared to the specimen with waveform 1. However, the specimen with waveform 2 demonstrates a 9.22% decrease in ductility but a 14.52% increase in bearing capacity. This phenomenon can be attributed to the fact that the specimen with waveform 3 distributes stress more uniformly, thereby enhancing both ductility and bearing capacity. In contrast, the specimen with waveform 2 improves bearing capacity to a certain extent, but it fails to sufficiently optimize the stress distribution, resulting in a reduction in ductility.

The stress distributions at distinct positions of corrugated steel plates with varying waveforms (waveform 1, 2, 3) were analyzed based on measuring points illustrated in Figure 13, where points A and B are located in the tensile area, and points D and E are located in the compressive area. Figure 13a presents the stress distribution curves of these points. As shown in Figure 13b, the transverse stress at the at-corrugation crest exhibits consistent trends during loading. In the tensile area, transverse stresses remain near zero during the initial stage. However, when the load reaches the peak bearing capacity, radial expansion of the steel tube imposes confinement pressure on the corrugated steel plate, leading to compressive stress at point A. As loading progresses, interfacial contact between the steel tube, concrete, and corrugated steel plate gradually deteriorates, causing the compressive stress to transition into tensile stress. In the compressive area, transverse stresses continuously increase throughout loading and retain elevated levels post failure, attributed to local buckling at the crest induced by concrete dilatancy. As illustrated in Figure 13c, the at-corrugation trough displays complementary characteristics to the at-corrugation crest: compressive area stresses approach zero, while tensile area stresses monotonically increase with loading. For waveform 3, the at-corrugation trough stress in the mid-region counterbalances the high-stress area at the at-corrugation crest, forming a mechanical equilibrium. This stress complementary mechanism validates the effectiveness of waveform optimization in improving cross-sectional stress uniformity.

Figure 13d,e reveals typical longitudinal stress distributions. During early loading, longitudinal stresses at the mid-region (point C) remain near zero. In the compressive area, longitudinal compressive stresses develop at both the at-corrugation crest and trough due to steel tube compression and in-plane deformation of the corrugated steel plate. Post-peak, significant tensile stresses emerge in the tensile side at-corrugation crest region, driven by tensile expansion of the steel tube, which induces interfacial delamination and slippage between the corrugated steel plate and core concrete. Importantly, waveform 3 exhibits higher longitudinal stresses compared to other waveforms, contributing additional bearing capacity to the lattice column.

Quantitative analysis reveals that when the peak load is reached, waveform 3 achieves maximum stress reductions of 70.13% in transverse stress and 70.26% in longitudinal stress compared to waveform 1 and waveform 2 at the wave crest. Similarly, at the wave trough, maximum reductions reach 76.82% for transverse stress and 53% for longitudinal stress. This significant reduction highlights its ability to mitigate localized stress concentrations, thereby delaying buckling initiation and enhancing stability under eccentric loading. These quantitative findings conclusively demonstrate that waveform 3 exhibits superior stress distribution characteristics.



(**a**) Distribution of points

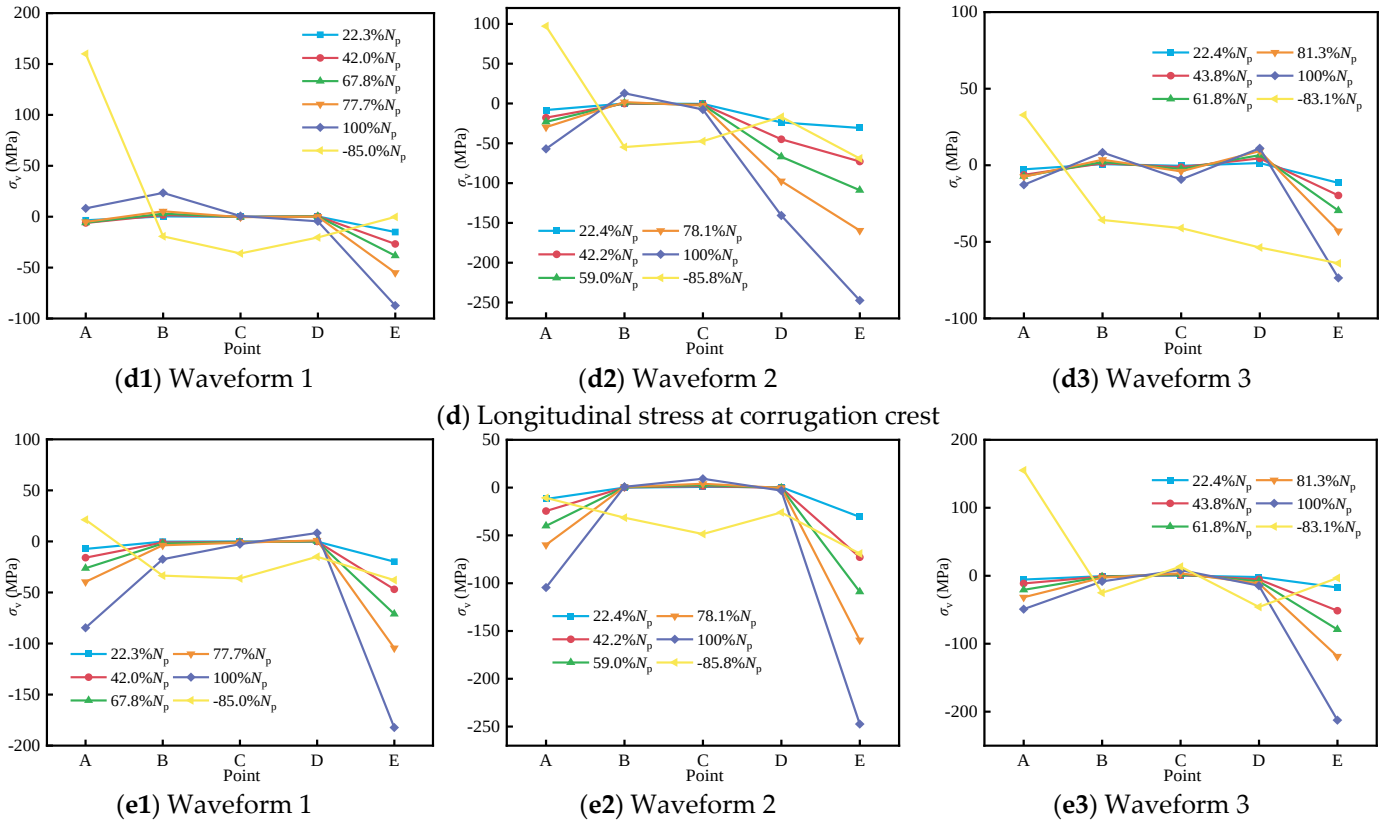
(**b1**) Waveform 1 (**b2**) Waveform 2 (**b3**) Waveform 3

(**b**) Transverse stress at corrugation crest

(**c1**) Waveform 1 (**c2**) Waveform 2 (**c3**) Waveform 3

(**c**) Transverse stress at corrugation trough

Figure 13. *Cont.*



(**d1**) Waveform 1 (**d2**) Waveform 2 (**d3**) Waveform 3

(**d**) Longitudinal stress at corrugation crest

(**e1**) Waveform 1 (**e2**) Waveform 2 (**e3**) Waveform 3

(**e**) Longitudinal stress at corrugation trough

Figure 13. Stress distribution of corrugated steel plate.

5. Bearing Capacity Calculation Method

For the novel latticed columns, the authors determined their axial load response and developed an analytical model for predicting the ultimate compressive capacity [3]. The derived formulation for the latticed column is presented in Equation (5):

$$N_{u0} = 2\alpha\varphi[(A_s f_s + A_{cs} f_{cs}) + A_{cr} f_{cr} + A_{ccr} f_{ccr}] \quad (5)$$

where α represents the correction factor addressing the effect of lacing tubes and corrugated plates on the latticed column's axial performance, and φ denotes the stability coefficient; A_s and f_s, respectively, denote the cross-sectional area and axial compressive resistance of square steel tubes; and A_{cs} and f_{cs} correspond to the cross-sectional dimensions and compressive strength of concrete infill within the tubes. For corrugated steel plate-encased concrete, A_{ccr} defines the effective cross-sectional area (take the average value at the trough position and the peak position), while f_{ccr} quantifies the compressive capacity of the concrete. Numerical simulations and prior investigations [3,29] reveal that corrugated steel plates contribute negligibly to axial load resistance, justifying their exclusion from the lattice column's axial load-bearing capacity formulation. The axial compressive strength equations for concrete-filled square tubes and corrugated plate composite sections are expressed as

$$f_{cs} = f_{co,cs}\left(-1.254 + 2.254\sqrt{1 + 7.94\frac{f_{r,cs}'}{f_{co,cs}}} - 2\frac{f_{r,cs}'}{f_{co,cs}}\right) \quad (6)$$

$$f_{ccr} = f_{co,ccr}\left(-1.254 + 2.254\sqrt{1 + 7.94\frac{f_{r,ccr}'}{f_{co,ccr}}} - 2\frac{f_{r,ccr}'}{f_{co,ccr}}\right) \quad (7)$$

where $f_{r,cs}{}'$ defines the effective confinement stress imposed by tubes on encapsulated concrete; $f_{r,\,ccr}$ characterizes the combined confinement from corrugated plates and tube walls; $f_{co,cs}$ refers to the axial compressive strength of concrete confined within tubes; and $f_{co,ccr}$ represents the axial compressive strength of concrete encapsulated in corrugated steel plates.

Under eccentric loading, lattice columns experience a significant reduction in load-bearing capacity due to combined effects including second-order phenomena (P-Δ effects), moment redistribution across cross-sections, and stability degradation. This study proposes an eccentricity reduction factor φ_e to express the eccentric compressive capacity N_u as a reduced form of the axial capacity N_{u0}:

$$N_{u0} = \varphi_e N_u \tag{8}$$

Based on P-Δ effects and stability principles, the correction formula is derived as

$$\varphi_e = \frac{1}{1 + k_1 (e_0/r)^2} \tag{9}$$

where e_0 is the eccentricity, r represents the radius of gyration, and k_1 characterizes the comprehensive modification coefficient for eccentric compression in the lattice columns. Through linear regression analysis, k_1 is determined as 4.35. Thus, the eccentric compressive capacity of the lattice column is calculated as

$$N_u = \varphi_e = \frac{1}{1 + k_1 (e_0/r)^2} N_{u0} \tag{10}$$

which is

$$N_u = \frac{2\alpha\varphi[(A_s f_s + A_{cs} f_{cs}) + A_{cr} f_{cr} + A_{ccr} f_{ccr}]}{1 + k_1 (e_0/r)^2} \tag{11}$$

The comparative analysis of theoretical predictions and numerical simulation results is presented in Table 4 and Figure 14. As evidenced by the data, the bearing capacity values derived from Equation (11) demonstrate satisfactory agreement with the finite element analysis results, with all computational deviations maintained below the 11% threshold. This close correlation between analytical and numerical approaches validates the reliability of the proposed formulation for engineering applications.

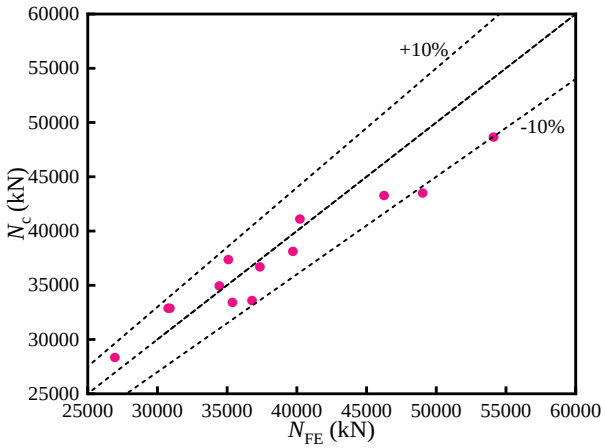


Figure 14. Calculated and simulated load capacity correlation analysis.

Table 4. Calculated and simulated results of specimens.

№	Specimen	N_c (kN)	N_{FE} (kN)	N_c/N_p
1	T1	32,876.62	30,892.8	1.06
2	E1	43,266.76	46,259.9	0.94
3	E2	41,101.83	40,224.3	1.02
4	E3	37,362.80	35,089.1	1.06
5	E4	28,339.61	26,942.5	1.05
6	C1	43,497.79	49,030.7	0.89
7	C2	48,657.56	54,117.7	0.90
8	H1	34,939.73	34,442.3	1.01
9	H2	36,685.44	37,349.8	0.98
10	H3	38,113.75	39,718.9	0.96
11	B1	33,409.89	35,379.9	0.94
12	B2	33,587.90	36,788.9	0.91
13	LQ1	32,876.62	30,771.4	1.07
14	LQ2	32,876.62	30,771.5	1.07
15	LQ3	32,876.62	30,771.5	1.07

Note: N_c denotes the analytical bearing capacity derived from Equation (11); N_{FE} signifies the simulated load-bearing capacity extracted via FE modeling.

6. Conclusions

This investigation evaluates the eccentric compressive behavior of lattice structural systems incorporating CFSTs and corrugated steel plates. A series of column specimens were designed with parametric variations to examine their structural performance. Systematic evaluation was conducted to assess the effects of key parameters on ultimate load capacity, deformation characteristics, and failure mechanisms under eccentric loading conditions. The principal research findings are presented below:

(1) Under eccentric loading, the latticed column exhibits typical bending failure characteristics, and the corrugated steel plate demonstrates a notable restraining effect under eccentric loading. The arrangement of diagonal lacing tubes optimizes the load distribution and enhances the overall bending resistance.

(2) Increasing eccentricity ratios induce a pronounced bending deformation and asymmetric stress/strain distribution. The results demonstrate up to a 41.8% reduction in load capacity but a 50.6% improvement in ductility. This behavior stems from eccentric loading limiting tensile area contributions while promoting compressive stress redistribution, with ductility gains ceasing beyond 350 mm of eccentricity.

(3) Higher steel strength enhances the stress redistribution in both tension and compression areas, increasing load capacity by 28.6% and ductility by 14.5%. Higher concrete strength increases the bearing capacity of the specimen, but decreases the ductility. Optimal performance requires an optimized steel–concrete composite action to achieve a better balance between load-bearing capacity and ductility.

(4) The geometric configuration of corrugated steel plates significantly influences plastic strain distribution and structural performance. Waveform 3 facilitates superior stress redistribution, enhancing both the bearing capacity of the specimen by 19.1% and the ductility by 9.7%. Optimal waveform selection is therefore critical for achieving balanced improvements in load-carrying and deformation-resistant capacities.

(5) Based on axial capacity formulas, an eccentric compression modification term for CFST-corrugated steel plate latticed columns was proposed. Comparative analysis reveals that the proposed method maintains calculation errors within 11% of numerical simulation results, verifying its reliability for eccentric loading conditions.

Author Contributions: X.-W.X.: methodology, conceptualization, supervision, and writing—original draft preparation. N.-N.Z.: formal analysis, software, and writing—review and editing. X.Z.: data curation and conceptualization. J.L.: methodology, resources, and funding acquisition. Z.-H.H.:

software and methodology. X.L.: software and data curation. All authors have read and agreed to the published version of the manuscript.

Funding: This research was supported by the Research and Development Project of CISDI Group Co., Ltd. (grant number: 90150915-KJ-001).

Data Availability Statement: The original contributions presented in this study are included in the article. Further inquiries can be directed to the corresponding author.

Conflicts of Interest: Authors Xue-Wen Xiao, Xuan Zhao and Zhao-Hui Hu were employed by CISDI Group Co., Ltd. Author Jun Liu was employed by XAUAT Engineering Technology Co., Ltd. The remaining authors declare that the research was conducted in the absence of any commercial or financial relationships that could be construed as a potential conflict of interest.

References

1. Kheyroddin, A.; Naderpour, H.; Ahmadi, M. Compressive strength of confined concrete in CCFST columns. *J. Rehabil. Civ. Eng.* **2014**, *2-1*, 106–113.
2. Wei, J.G.; Han, J.P.; Luo, X.; Yang, Y.; Li, C.; Wang, W.R. Axial compression performance of ultra-high-strength concrete filled steel tubular lattice short columns. *J. Constr. Steel Res.* **2024**, *216*, 108571. [CrossRef]
3. Yang, Y.F.; Liu, M.; Hou, C.; Bie, X.M. Behaviour of four-legged square CFST latticed members under lateral cyclic loading. *J. Constr. Steel Res.* **2019**, *156*, 54–74. [CrossRef]
4. Zhao, X.; Zhang, N.; Hu, Z.; Li, X.; Nie, Y.; Liu, J. Axial compression behavior of novel latticed columns with CFST tubes and corrugated steel plates for industrial structures. *Buildings* **2025**, *15*, 42. [CrossRef]
5. Yang, Z.M.; Chen, J. Behavior of eccentrically loaded large-scale CFST slender columns with latticed annular steel. *Structures* **2024**, *69*, 107451. [CrossRef]
6. Huang, Z.; Li, X.; Chen, J.; Jiang, L.; Chen, Y.F.; Huang, Y. Research on seismic performance prediction of CFST latticed column-composite box girder joint based on machine learning. *Constr. Build. Mater.* **2025**, *460*, 139811. [CrossRef]
7. Gu, C.; Wang, X.; Liu, Y.; Zhou, X.; Huang, C. Conceptual design and analysis on an innovative hybrid CFST latticed bridge pier with an RC lacing system. *Structures* **2025**, *73*, 108309. [CrossRef]
8. Zeng, W.; Ayough, P.; Zhou, X.H.; Wang, Y.H.; Ren, W.; Elchalakani, M.; Elghazouli, A.Y. Performance of circular CFST columns strengthened with CFRP grid-reinforced ECC under axial compression: Numerical modelling and design. *Eng. Struct.* **2025**, *325*, 119375. [CrossRef]
9. Wei, J.G.; Han, J.P.; Luo, X.; Yang, Y.; Li, C. Eccentric load capacity of ultra-high strength concrete-filled steel tubular lattice short columns. *Structures* **2024**, *69*, 107385. [CrossRef]
10. Jiang, L.Z.; Zhou, W.B.; Wu, Z.Y.; Zhang, J.J. Experimental study and theoretical analysis on the ultimate load carrying capacity of four-tube concrete filled steel tubular lattice columns. *China Civ. Eng. J.* **2010**, *43*, 55–62.
11. Nie, J.G.; Liao, Y.B. Experiments of four-legged concrete filled steel tubular laced columns subjected to axial loads. *Tsinghua Sci. Technol.* **2009**, *49*, 1919–1924.
12. Chen, B.C.; Ou, Z.J. Experimental study on influence of slenderness ratio in concrete filled steel tubular laced columns under eccentric compression. *J. Build. Struct.* **2006**, *27*, 73–79.
13. Ou, Z.J.; Chen, B.C. Experimental research on influence of eccentrically ratio on concrete filled steel tubular laced columns compressed eccentrically. *J. Build. Struct.* **2007**, *28*, 184–190.
14. Liao, X.; Li, X.; Li, W.; Su, R.; Chen, M. Seismic behavior of CFST components for shear walls using double corrugated steel plates. *Eng. Struct.* **2025**, *334*, 120235. [CrossRef]
15. Shi, Y.; Sun, C.; Gao, C.; Liu, J.; Peng, X. Study on lateral resistance of cold-formed corrugated steel plates with lightweight foam concrete composite walls. *Thin-Walled Struct.* **2025**, *210*, 112964. [CrossRef]
16. Wu, R.M.; Tong, J.Z. Shear strength and post-ultimate behavior of multi-stiffened corrugated steel plate shear walls. *J. Constr. Steel Res.* **2025**, *229*, 109480. [CrossRef]
17. Dou, C.; Xie, C.; Wang, Y.; Yang, N. Cyclic loading test and lateral resistant behavior of flat-corrugated steel plate shear walls. *J. Build. Eng.* **2023**, *66*, 105831. [CrossRef]
18. Bi, Z.J.; Yang, G.T. Buckling of corrugated steel plates under uniaxial compression. *J. Constr. Steel Res.* **2024**, *223*, 109074. [CrossRef]
19. Elkawas, A.A.; Hassanein, M.F.; El Hadidy, A.M.; El-Boghdadi, M.H.; Elchalakani, M. Behaviour of corrugated web girders subjected to lateral-torsional buckling: Experimental tests and numerical modelling. *Structures* **2021**, *33*, 152–168. [CrossRef]
20. Shariatyazdi, P.; Ronagh, H.; Izadinia, M.; Javaheritafti, M.R. Shear buckling behavior of tapered cantilever beams with corrugated trapezoidal web under concentrated tip load. *J. Constr. Steel Res.* **2022**, *193*, 107265. [CrossRef]

21. Wang, C.Y.; Yin, S.P.; Wang, B.X.; Du, J.; Ren, X.; Zhang, X. Research on the transverse flexural performance of T-PBL joints between corrugated steel webs and concrete slabs. *Structures* **2022**, *44*, 1057–1069.
22. Alikhanifard, M.A.; Rahai, A.R.; Tehrani, P. A new shear strength model for steel corrugated web girders. *J. Constr. Steel Res.* **2022**, *197*, 107457. [CrossRef]
23. Liu, W.; Han, L.H. Research on some issues of ABAQUS analysis on the behavior of axially loaded concrete-filled steel tubes. *J. Harbin Inst. Technol.* **2005**, *37*, 157–160.
24. Esmaeily, A.; Xiao, Y. Behavior of reinforced concrete columns under variable axial loads: Analysis. *ACI Struct. J.* **2005**, *102*, 736–744.
25. Yu, H.L.; Jeong, D.Y. Application of a stress triaxiality dependent fracture criterion in the finite element analysis of unnotched Charpy specimens. *Theor. Appl. Fract. Mech.* **2010**, *54*, 54–62. [CrossRef]
26. Bao, Y.B.; Wierzbicki, T. On fracture locus in the equivalent strain and stress triaxiality space. *Int. J. Mech. Sci.* **2004**, *46*, 81–98. [CrossRef]
27. Zhang, S.J.; Zou, Y.; Wang, C.Q.; Wu, Y.C.; Chen, M. Behaviour and bearing capacity of concrete-filled horizontal corrugated steel plate-tubular composite columns under biaxial eccentric compression. *Eng. Mech.* **2021**, *38*, 81–90.
28. Su, R.; Li, X.; Chen, M.; Yan, H.; Wu, Y.C. Confinement mechanism of angle steel-corrugated steel plate confined concrete columns under compression. *J. Constr. Steel Res.* **2025**, *230*, 109547. [CrossRef]
29. Sun, Z.X. Study on Axial Compression Behavior and Confinement Mechanism of Steel Tubular-Corrugated Steel Plate Concrete Columns. Master's Thesis, Jiangnan University, Wuxi, China, 2023.

Disclaimer/Publisher's Note: The statements, opinions and data contained in all publications are solely those of the individual author(s) and contributor(s) and not of MDPI and/or the editor(s). MDPI and/or the editor(s) disclaim responsibility for any injury to people or property resulting from any ideas, methods, instructions or products referred to in the content.